

# Visible and dark matter in M 31 - II. A dynamical model and dark matter density distribution

E. Tempel<sup>1,2\*</sup>, A. Tamm<sup>1</sup> and P. Tenjes<sup>1,2</sup>

<sup>1</sup>*Tartu Observatory, 61602 Tõravere, Estonia*

<sup>2</sup>*Institute of Theoretical Physics, Tartu University, Tähed 4, 51050 Tartu, Estonia*

Accepted 2008 Month 00, Received 2007 Month 00.

## ABSTRACT

In the present paper we derive the density distribution of dark matter (DM) in a well-observed nearby disc galaxy, the Andromeda galaxy. From photometrical and chemical evolution models constructed in the first part of the study (Tamm, Tempel & Tenjes 2008, hereafter Paper I) we can calculate the mass distribution of visible components (the bulge, the disc, the stellar halo, the outer diffuse stellar halo). In the dynamical model we calculate stellar rotation velocities along the major axis and velocity dispersions along the major, minor and intermediate axes of the galaxy assuming triaxial velocity dispersion ellipsoid. Comparing the calculated values with the collected observational data, we find the amount of DM, which must be added to reach an agreement with the observed rotation and dispersion data.

We conclude that within the uncertainties, the DM distributions by Moore, Burkert, Navarro, Frenk & White (NFW) and the Einasto fit with observations nearly at all distances. The NFW and Einasto density distributions give the best fit with observations.

The total mass of M 31 with the NFW DM distribution is  $1.19 \cdot 10^{12} M_{\odot}$ , the ratio of the DM mass to the visible mass is 10.0. For the Einasto DM distribution, these values are  $1.28 \cdot 10^{12} M_{\odot}$  and 10.8. The ratio of the DM mass to the visible mass inside the Holmberg radius is 1.75 for the NFW and the Einasto distributions. For different cuspy DM distributions, the virial mass is in a range  $(6.9-7.9) \cdot 10^{11} M_{\odot}$  and the virial radius is  $\sim 150$  kpc. The DM mean densities inside 10 pc for cusped models are 33 and  $16 M_{\odot} \text{pc}^{-3}$  for the NFW and the Einasto profiles, respectively. For the cored Burkert profile, this value is  $0.06 M_{\odot} \text{pc}^{-3}$ .

**Key words:** galaxies: individual: Andromeda, M 31 – galaxies: kinematics and dynamics – dark matter.

## 1 INTRODUCTION

Models of hierarchical merging of cold dark matter describe rather well the observed general properties of galaxies, large-scale structure of clusters, superclusters and their network.

On the other hand, the observed number of dwarf galaxies seems to be too small in comparison with cold dark matter models. But by far the most commonly referred contradiction is related to disc galaxies. Cosmological simulations generate dark matter (DM) haloes with central density cusps of  $\rho \sim r^{-1}$  or steeper (e.g. Navarro, Frenk & White 1997; Moore et al. 1999). Observations of dwarf and low surface brightness disc galaxies have usually shown that shallow central density profiles fit the data better than cuspy profiles (Moore 1994; Burkert 1995; Blais-Ouellette, Am-

ram & Carignan 2001; Borriello & Salucci 2001; de Blok, McGaugh & Rubin 2001; de Blok & Bosma 2002; Salucci, Walter & Borriello 2003; Wdredake, de Blok & Walter 2003; Simon et al. 2005; Zackrisson et al. 2006; Kassin, de Jong & Weiner 2006; Gentile et al. 2004, 2007; Valenzuela et al. 2007). Observational data are consistent with cuspy density profiles only for a few objects (e.g. Swaters et al. 2003; de Blok 2005; Simon et al. 2005).

Discrepancy between the predicted cuspy DM density profiles and the observed rotation curves with shallow profiles has been explained with limited resolution of rotation curves and non-circular motions of gas and with the statement that the actual contribution of visible stellar matter is poorly known.

The aim of the present paper is to derive the density distribution of dark matter in a nearby disc galaxy, the Andromeda galaxy. The galaxy M 31 was selected be-

\* E-mail: elmo@aai.ee; atamm@ut.ee; peeter.tenjes@ut.ee

cause (1) photometrical and kinematical (rotation, dispersions) data are measured with sufficiently high resolution in order to study the bulge region; (2) velocity dispersions have been measured also outside the galactic apparent major axis; in addition to stellar kinematics, the kinematics of planetary nebulae (PN) is known; (3) direct measurements of metallicities allow to constrain the mass-to-light ( $M/L$ ) ratios of visible matter; (4) independent estimates of the mass distribution on large scales are available (globular clusters (GC), satellites, stream, kinematics of the Milky Way + M 31 system).

In the first part of the study (Paper I), we constructed the photometrical model of M 31 stellar populations on the basis of surface brightness profiles in  $U$ ,  $B$ ,  $V$ ,  $R$ ,  $I$  and  $L$  colours (see also Tenjes, Haud & Einasto 1994). The derived photometrical model gives us parameters of galactic components, colour indices among them. From independent spectral observations, the metallicity of the stellar content is available. The colour indices and the metallicity of each component were interpreted with the help of chemical evolution models to calculate the ages and  $M/L$ -ratios of the components. In total, the output of the first paper were density distribution parameters, ages and  $M/L$ -ratios of galactic components.

In the present paper, we apply the results of Paper I and construct a mass distribution model of M 31 consistent with the measured kinematics. Stellar components and their  $M/L$ 's together with the photometrical model give us the mass distribution of visible matter. Calculating the rotation velocities and velocity dispersions of visible matter with the help of the dynamical model (see Tempel & Tenjes 2006) the amount of DM can be found, which must be added to reach an agreement with the observed rotation and dispersion data.

In principle, to derive the DM density distribution, it is not necessary to take into account stellar velocity dispersions. It is sufficient to compare the gas rotation curve with the calculated derivatives of the gravitational potential. This simple and straightforward method is frequently used. Of course, before calculations the gas rotation curve must be corrected for possible expansion velocities, non-circular motions and dispersions (see Gentile et al. 2007). However, one of the most uncertain aspects of this method is the  $M/L$  of the visible matter. Chemical evolution models involve several insufficiently constrained parameters. It is possible to decrease degeneracy by using 3–5 different colour indices, but due to measurement uncertainties, colour indices are often controversial. The comparison of the results with additional and independent observations (stellar rotation curve, velocity dispersions along several slit-positions) allows us to constrain the distributions of visible matter and thereafter DM.

In the present model, we assume that a galaxy is a superposition of ellipsoids of rotation with different flattening. We assume that stellar populations have both rotation and dispersion components. The velocity dispersion ellipsoid of visible matter is triaxial. DM has spherical density distribution and is collision-free.

The general scheme of Paper I and Paper II (present paper) is given in Fig. 1. The photometrical model and the chemical evolution model constitute the first part of the study and depend very strongly on each other. The output of

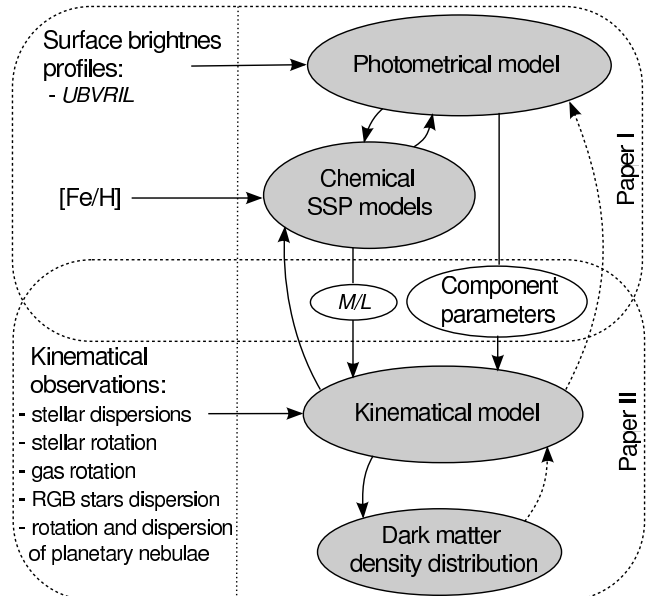


**Figure 1.** The principle scheme of the construction of the M 31 model in the framework of Paper I and Paper II (the present paper). The arrows show dependencies between different model construction stages. The dashed arrows represent weaker impact.

the first part (component parameters and  $M/L$ -ratios) is the input to the second part of the study. At the second stage, we use the kinematical model and narrow down the output of the first part. Finally, we get a self-consistent model and derive the DM density distribution, using a possibly wide variety of observational data.

In Section 2, we describe the observational data which we have used. Kinematical data consist of gas rotation, stellar rotation and dispersions, rotation velocities and dispersions of PN and velocity dispersions of individual red giant branch (RGB) stars. In Section 3, the dynamical model and an algorithm for calculating the DM distribution are described. In Sections 4 and 5, visible and DM density distributions are derived and compared with available observational data. In Section 6, the results are discussed.

The general parameters of M 31 used in the present paper are: the system velocity is  $-300 \text{ km s}^{-1}$  (de Vaucouleurs et al. 1991; van den Bergh 2000), the galaxy inclination angle is  $77.5^\circ$  (Walterbos & Kennicutt 1988; de Vaucouleurs et al. 1991), the major axis position angle is  $38.1^\circ$  (Walterbos & Kennicutt 1987; Ferguson et al. 2002) and the distance has been taken 785 kpc (McConnachie et al. 2005), corresponding to the scale  $1 \text{ arcmin} = 228 \text{ pc}$ . Throughout the paper we use the  $\Lambda$ CDM cosmological model with  $\Omega_m = 0.3$  and  $H_0 = 75 \text{ km s}^{-1} \text{ Mpc}^{-1}$ .

## 2 OBSERVATIONAL DATA

In Paper I we described photometrical and chemical composition data used to construct the photometrical model. In the present section, we describe kinematical data, used for the construction of the dynamical model. From a large variety of kinematical information, we present only the observations, that can be compared with our model output.

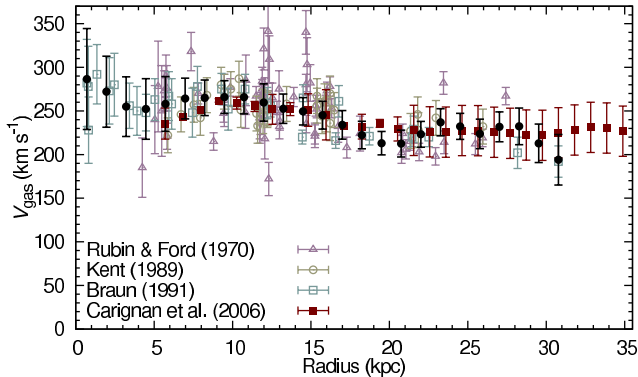


**Figure 2.** Circular velocity, derived from H I and H II observations. The filled circles are averaged rotational velocities obtained using the data from earlier observations (faint points). The filled squares are recent H I observations by Carignan et al. (2006). See the text for more information.

**Table 1.** References for rotation and dispersion data along the major and the minor axis.

Reference	$R_{\max}$ [kpc]	$z_{\max}$ [kpc]
McElroy (1983)	2.27	1.98
Kormendy (1988)	0.185	–
van der Marel et al. (1994)	0.234	0.16
Kormendy & Bender (1999)	0.18	–

## 2.1 H I and H II observations

We constructed the gas rotation curve of M31 on the basis of H II observations by Rubin & Ford (1970) and H I observations by Kent (1989) and Braun (1991). Observational data points from these studies were averaged, and the resulting rotation velocities are presented by filled circles in Fig. 2. To calculate the error-bars, a bootstrap method is used, combining the bootstrap errors with observational errors.

In outer parts of M31, an extended H I rotation curve has recently been measured by Carignan et al. (2006). They measured the rotation curve outside 90 arcmin, between 20 and 35 kpc, and recomputed also rotation velocities, using earlier H I data by Unwin (1983). Rotational velocities by Carignan et al. (2006) are shown by filled squares in Fig. 2. The derived rotation curve represents gas kinematics from 1–35 kpc.

## 2.2 Stellar velocity and dispersion observations

The intrinsic structure of the nucleus of M31 is not clear – it may have a ringlike and/or a double or even a triple structure (Lauer et al. 1993; Geressen, Kuijken & Merrifield 1995; Peiris & Tremaine 2003; Salow & Statler 2004; Bender et al. 2005). In the context of the present paper, the contribution of the nucleus is unimportant, we look at regions outside 0.01 kpc and we exclude the nucleus from our model.

Stellar rotation velocities and velocity dispersions in the central regions of M31 have been measured by several authors (see references in Tenjes et al. 1994). To model the contribution of visible and DM to the total mass distribution, it is useful to possess kinematical data outside the galactic

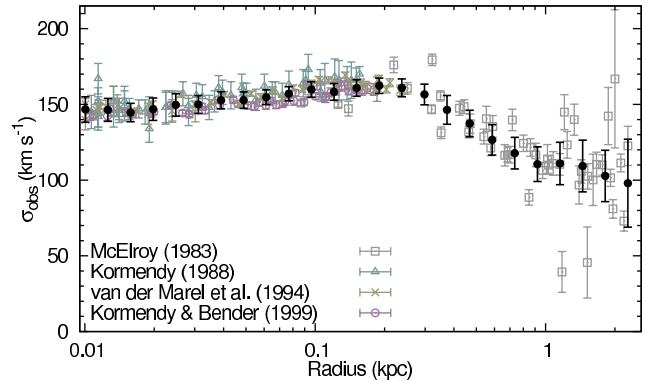


**Figure 3.** Stellar dispersion observations. The faint points correspond to observations from different authors. The filled circles denote the averaged profile.

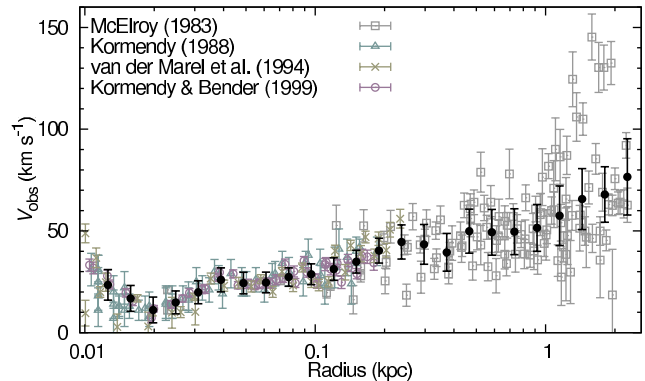


**Figure 4.** Stellar rotational velocities. The faint points are observations from different authors. The filled circles denote the averaged profile.

apparent major axis and at largest distance intervals (see Tempel & Tenjes 2006). References to stellar kinematical data used in the present paper are presented in Table 1 which also gives maximal distances along the major and the minor axis. McElroy (1983) measured stellar rotation and dispersions up to the distances of 2.3 kpc from the centre along 12 cuts (at every 15°) that penetrate the galaxy centre. None of them was exactly along the galactic major (minor) axis, and for this reason, we averaged two cuts at 6.8° and 8.1° from the major (minor) axis. Observations by other authors were sufficiently close to the major (minor) axis.

Velocity dispersions and rotation velocities along the major axis are presented in Figs. 3 and 4, respectively. Individual observations have been averaged; for error-bars a bootstrap method was used, combining bootstrap errors with observational errors. Outside the major and the minor axis, the observations by McElroy (1983) were combined into four cuts at 23°, 38°, 53° and 68° from the major axis and they are shown by filled circles in Fig. 10.

## 2.3 Planetary nebulae observations

Kinematical observations for PN have been published by Halliday et al. (2006); Merrett et al. (2006). Halliday et al. (2006) used 50 nebulae for every data point and Merrett

et al. (2006) used roughly 40 nebulae. For every data point, they have found the averaged velocity and dispersion near the galactic major axis.

In our model, we handle the kinematics of PN in a similar way to the kinematics of the stellar component. As a result, the stellar observations give us the kinematics in inner parts of the galaxy and PN observations give the kinematics mainly in outer parts. In overlapping regions both data are in accordance.

## 2.4 Observations of red giant branch (RGB) stars.

Reitzel & Guhathakurta (2002) observed the kinematics of RGB stars along the minor axis. At a distance of 19 kpc from the centre, the calculated velocity dispersion was found to be  $150_{-30}^{+50} \text{ km s}^{-1}$ . Kalirai et al. (2006) measured 106 RGB stars at 12 kpc along the minor axis and the derived dispersion was  $90 \text{ km s}^{-1}$ . The most recent observations by Gilbert et al. (2007) involved distances in the range of 9–30 kpc along the minor axis. They measured RGB stars in different fields and the averaged dispersion in this region is  $129 \text{ km s}^{-1}$ . The results from different fields and errors are presented in Fig. 9.

Chapman et al. (2006) made observations of RGB stars along the major axis in the halo region (10–70 kpc). They made spectroscopic observations for 827 stars. The main conclusion was that the halo sample shows no significant evidence for rotation. They measured the central dispersion  $152 \text{ km s}^{-1}$ , which decreases with radius. The observed dispersions by Chapman et al. (2006) are higher than stellar or PN observations. There is no strict explanation for that, but probably the line-of-sight velocity component is not correctly subtracted, and therefore the dispersions are higher. Also, there is a possibility that RGB stars have systematically higher dispersions. Unfortunately, in our final model we cannot compare these observations with our model output.

## 3 A DYNAMICAL MODEL

### 3.1 Calculation of stellar velocities and dispersions

Details of the dynamical model described below can be found in Tempel & Tenjes (2006). However, to improve the readability of the paper, a brief outline is given here.

#### 3.1.1 Basic formulae

Let  $(R, z, \theta)$  be cylindrical coordinates and  $a = \sqrt{R^2 + z^2/q^2}$ , where  $q$  is the axial ratio of isodensity ellipsoids. Knowing spatial luminosity densities of the components  $l_i(a)$  and ascribing a  $M/L$ -ratio to each component  $f_i$  ( $i$  indexes the bulge, the disc, the stellar halo and the outer diffuse stellar halo; see Paper I), we obtain the spatial mass density distribution of a galaxy

$$\rho(a) = \sum_{i=1}^5 f_i l_i(a) + \rho_{\text{DM}}(a) \quad (1)$$

( $\rho_{\text{DM}}(a)$  is the DM density). On the basis of spatial mass density distributions, derivatives of the gravitational potential  $\frac{\partial \Phi}{\partial R}$  and  $\frac{\partial \Phi}{\partial z}$  can be calculated.

In stationary collisionless stellar systems with axial-symmetry the Jeans equations in cylindrical coordinates can be written in a convenient form for further calculations

$$\frac{\partial \rho \sigma_R^2}{\partial R} + \left( \frac{1-k_\theta}{R} + \frac{\partial \kappa}{\partial z} \right) \rho \sigma_R^2 + \kappa \frac{\partial \rho \sigma_R^2}{\partial z} = -\rho \frac{\partial \Phi}{\partial R} (1-\beta^2), \quad (2)$$

$$\frac{\partial \rho \sigma_z^2}{\partial z} + \left( \frac{\xi}{R} + \frac{\partial \xi}{\partial R} \right) \rho \sigma_z^2 + \xi \frac{\partial \rho \sigma_z^2}{\partial R} = -\rho \frac{\partial \Phi}{\partial z}, \quad (3)$$

where

$$\kappa \equiv \frac{1-k_z}{2} \tan(2\alpha), \quad \xi \equiv \frac{\kappa}{k_z}, \quad (4)$$

$$k_z \equiv \frac{\sigma_z^2}{\sigma_R^2}, \quad k_\theta \equiv \frac{\sigma_\theta^2}{\sigma_R^2}. \quad (5)$$

$\alpha$  is the angle between the major axis of the velocity dispersion ellipsoid and the galactic plane. For each component, the rotation velocity has been taken  $V_\theta = \beta V_c$ , where  $V_c$  is circular velocity and  $\beta$  is a constant specific for each subsystem.

The Jeans equations (2) and (3) contain unknown functions  $k_z$ ,  $k_\theta$  and  $\alpha$ . In our model, the phase-density of a system is a function of three integrals of motion. Under this assumption, we can derive the unknown functions.

From the Jeans equations (2) and (3) the dispersions along the coordinate axis ( $\sigma_R$ ,  $\sigma_z$  and  $\sigma_\theta$ ) can be calculated

$$\rho \sigma_R^2(R, z) = (1-\beta^2) \int_R^\infty \rho \frac{\partial \Phi(r, z)}{\partial R} \left[ \exp \int_R^r p(r^*, z) dr^* \right] dr, \quad (6)$$

$$\rho \sigma_z^2(R, z) = \int_z^\infty \rho \frac{\partial \Phi(R, z')}{\partial z} \left[ \exp \int_z^{z'} g(R, z^*) dz^* \right] dz', \quad (7)$$

$$\sigma_\theta^2 = k_\theta \sigma_R^2 \quad \text{or} \quad \sigma_\theta^2 = \frac{k_\theta}{k_z} \sigma_z^2, \quad (8)$$

where

$$p \equiv \frac{1-k_\theta}{R} + \frac{\partial \kappa}{\partial z}, \quad g \equiv \frac{\xi}{R} + \frac{\partial \xi}{\partial R}. \quad (9)$$

The details of derivation and some restrictions can be found in Tempel & Tenjes (2006).

#### 3.1.2 Line-of-sight dispersions

Calculated velocity dispersions  $\sigma_R^2$ ,  $\sigma_z^2$  and  $\sigma_\theta^2$  cannot be directly compared with observations. The calculated dispersions must be projected to the line-of-sight. Designating  $\Theta$  as the angle between the line-of-sight and the galactic plane (see Fig. 5), the line-of-sight dispersions  $\sigma_{\text{los}}^2$  are

$$\sigma_{\text{los}}^2 = \sigma_*^2 \cos^2 \Theta + \sigma_z^2 \sin^2 \Theta, \quad (10)$$

where

$$\sigma_*^2 = \sigma_\theta^2 \frac{X^2}{R^2} + \sigma_R^2 \left( 1 - \frac{X^2}{R^2} \right). \quad (11)$$

The next step is to integrate individual line-of-sight velocity components along the whole line-of-sight

$$\sigma_{\text{int}}^2(X, Y) = \frac{1}{L(X, Y)} \int_X^\infty R \frac{\sum_{i=1}^2 [l(R, z_i) \sigma_{\text{los}}^2(R, z_i)]}{\cos \Theta \sqrt{R^2 - X^2}} dR, \quad (12)$$

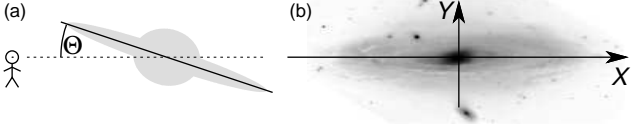


**Figure 5.** Panel (a) gives the angle between the line-of-sight and the galactic plane. Panel (b) shows our galactic coordinates  $X$  and  $Y$  in the sky.

$$z_{1,2} = \left( \frac{Y}{\sin \Theta} \pm \sqrt{R^2 - X^2} \right) \tan \Theta, \quad (13)$$

where  $l(R, z)$  denotes galactic spatial luminosity density, and  $L(X, Y)$  is the surface luminosity density profile.

Equation (12) gives the line-of-sight dispersion for one galactic component. Our model consists of several components and we must sum over all components considering the surface luminosity profile

$$\sigma_{\text{obs}}^2(X, Y) = \frac{\sum_i \{L_i(X, Y) [\sigma_{\text{int}}^2(X, Y)]_i\}}{\sum_i L_i(X, Y)}, \quad (14)$$

where  $i$  denotes the subsystem and the summation is taken over all subsystems.

### 3.1.3 Line-of-sight stellar velocities

In an axisymmetric system, we have only one velocity component, the rotational velocity  $V_\theta$ . According to the definition of the circular velocity, we can write for each component (Binney & Tremaine 1987, equation (2.19))

$$V_\theta^2 = \beta^2 R \frac{\partial \Phi}{\partial R} = \beta^2 4\pi G q \int_0^R \frac{\rho(a) x^2 dx}{\sqrt{R^2 - e^2 x^2}}, \quad (15)$$

where  $a^2 = x^2 + z^2 x^2 (R^2 - e^2 x^2)^{-1}$  and  $e = \sqrt{1 - q^2}$  is eccentricity. The rotational velocity cannot be compared directly to the observed velocity. We use the same projection method for stellar velocities as we used for dispersions. The projected line-of-sight velocity is

$$V_{\text{los}} = V_\theta \frac{X}{R} \cos \Theta. \quad (16)$$

The observable velocity  $V_{\text{obs}}$  is

$$V_{\text{obs}}(X, Y) = \frac{\sum_i \{L_i(X, Y) [V_{\text{int}}(X, Y)]_i\}}{\sum_i L_i(X, Y)}, \quad (17)$$

where  $V_{\text{int}}$  is the same as the right-hand side of equation (12), only  $\sigma_{\text{los}}^2 \equiv V_{\text{los}}^2$ . The summation is taken over all subsystems.

## 3.2 Calculation of dark matter distribution

Total gravitational potential is a sum of the potentials caused by visible matter and DM. In terms of circular velocities,

$$V_c^2 = V_c^{\text{vis}} + V_{\text{DM}}^2. \quad (18)$$

Photometrical and chemical evolution models give us the spatial mass density of visible matter (see equation (1))

and thereafter  $V_c^{\text{vis}}$ . If gas velocity dispersions are small in comparison with rotation velocities and we neglect also non-circular motions, gas rotation velocities can be identified with total circular velocities and equation (18) gives us the spatial mass density distribution of DM

$$\rho_{\text{DM}}(R) = \frac{1}{4\pi R^2 G} \frac{d}{dR} \left( R V_{\text{DM}}^2 \right) \quad (19)$$

and inner mass of DM

$$M_{\text{DM}}(R) = \frac{R V_{\text{DM}}^2}{G}, \quad (20)$$

where  $G$  is the gravitational constant.

Unfortunately, this straightforward calculation is too simplified. In the most interesting bulge region, ignoring of non-circular motions and dispersions of the gas is not justified. For this reason, total circular velocities remain unknown and we must use another way to calculate the DM density.

In a simple form, the first Jeans equation (2) can be written as

$$V_c^2 = V_\theta^2 + \sigma_R^2 f(R), \quad (21)$$

where  $f(R)$  is a specific function. Applying (21) for total matter (visible + DM), we have

$$V_c^2 = V_\theta^2 + \sigma_R^2 f(R). \quad (22)$$

Substituting the last equation into equation (18), we get

$$V_{\text{DM}}^2 = V_\theta^2 - V_c^2 + \sigma_R^2 f(R), \quad (23)$$

where  $\sigma_R^2$  and  $V_\theta^2$  are the observed velocity dispersion and the observed rotational velocity, respectively. The circular velocity of the visible matter results from the component parameters derived in Paper I. It is reasonable to assume that the function  $f(R)$  is the same for total matter and for visible matter (DM is collision-free). Taking this into account,

$$V_c^2 = V_\theta^2 + \sigma_R^2 f(R). \quad (24)$$

Expressing from the previous equation  $f(R)$ , we can write

$$f(R) = \frac{V_c^2 - V_\theta^2}{\sigma_R^2}, \quad (25)$$

where  $V_\theta^2$  and  $\sigma_R^2$  are the visible matter rotational velocity and dispersion, respectively. We can find these quantities, using the method described in Section 3.1. Substituting equation (25) into equation (23), we finally get the DM circular velocity

$$V_{\text{DM}}^2 = V_\theta^2 - V_c^2 + \frac{\sigma_R^2}{\sigma_{\text{vis}}^2} \left( V_c^2 - V_\theta^2 \right). \quad (26)$$

Using equations (19), (20) and (26), we find the DM density distribution and the inner mass of DM, taking into account the rotation and dispersion data.

Rotational velocities and dispersions in equation (26) must be determined in the galactic equatorial plane as a function of radius.

The Jeans equation in form (21) is not entirely correct, because we did not consider dispersion derivatives. To have the correct form, an additional term must be added to the right-hand side

$$-R \left[ \frac{\sigma^2}{\rho} \frac{\partial \rho}{\partial R} + \frac{\partial \sigma^2}{\partial R} \right]. \quad (27)$$

Taking this correction into account, also a correction to the right-hand side of equation (26) must be added

$$R \left[ \frac{\sigma_{\text{obs}}^2}{\sigma_{\text{vis}}^2} \frac{\partial \sigma_{\text{vis}}^2}{\partial R} - \frac{\partial \sigma_{\text{obs}}^2}{\partial R} \right] + R \sigma_{\text{obs}}^2 \left[ \frac{1}{\rho_{\text{vis}}} \frac{\partial \rho_{\text{vis}}}{\partial R} - \frac{1}{\rho_{\text{tot}}} \frac{\partial \rho_{\text{tot}}}{\partial R} \right]. \quad (28)$$

This additional term is important only on a small scale. We cannot adequately consider the derivatives of dispersions as numerical differentiation amplifies noises in observational data too much, and therefore we do not use this term in our calculation.

#### 4 MASS DISTRIBUTION MODEL OF M 31

We assume M 31 to consist of the following subsystems: a bulge, a disc, a stellar halo, an outer diffuse stellar halo and a DM halo. Reasoning of the component selection (except DM halo) and their parameters resulting from the photometrical model are given in table 1 in Paper I. Luminosity distributions of the components are transformed to mass distributions on the basis of  $M/L$ 's resulting from chemical evolution models. Chemical evolution models give the components most probable  $M/L$  in different colours and possible  $M/L$  ranges.

As most kinematical observations have been made at wavelengths close to the  $V$ -band, the  $V$ -luminosities are used in weighting the components if superposition is needed (Equations (14) and (17)). Component parameters most relevant in context of the present paper are given in Table 2. According to Nietten et al. (2006), we add to the disc a total neutral gas mass  $5.2 \cdot 10^9 M_{\odot}$ .

Dynamical models can further constrain the permitted mass intervals. In our dynamical modelling process, we tried many different models, and, in most cases, the main conflict was that chemical evolution models predict larger bulge masses than dynamical models permit. The masses of other components remain between the permitted values. In our final dynamical model, masses for the disc, the stellar halo and the outer diffuse stellar halo are in accordance with the masses from the chemical evolution model. To achieve the correct concentration parameter for the NFW dark matter halo, we slightly decreased the best disc mass resulting from the chemical evolution models. The bulge mass in our final model is also slightly smaller than the minimal stellar mass predicted by the chemical evolution model. The smaller bulge mass was needed for an agreement with the observed velocity dispersion data in the bulge region.

In addition to masses, dynamical models contain a parameter  $\beta$ . This parameter was, in fact, determined for each component on the basis of fitting the stellar and PN rotation velocities with the model. On the other hand, an increasing of rotation velocities causes a decrease of velocity dispersions. In this way also dispersions influence the determination of  $\beta$ . Final values of  $\beta$  parameters are given in Table 2.

Circular velocities for visible and DM components in the final model are given in Fig. 6 as dashed lines. For comparison, observed gas rotation velocities are given by filled circles and filled squares. Our model is in good agreement with observations.

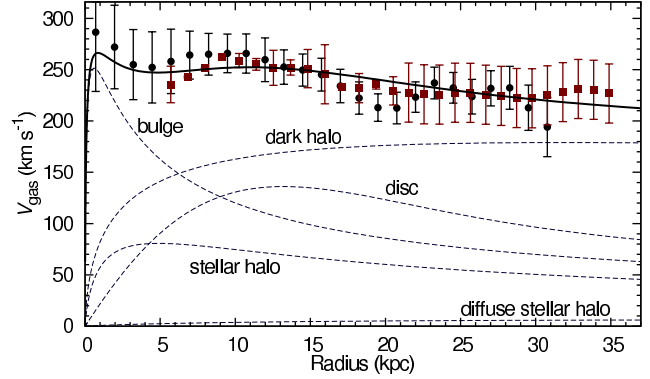


**Figure 6.** Gas rotational velocity. The filled circles are an averaged profile (see Fig. 2), the filled squares show the rotation curve from Carignan et al. (2006). The solid line denotes circular velocity derived from our model. The dashed lines show the rotational velocity for different components.

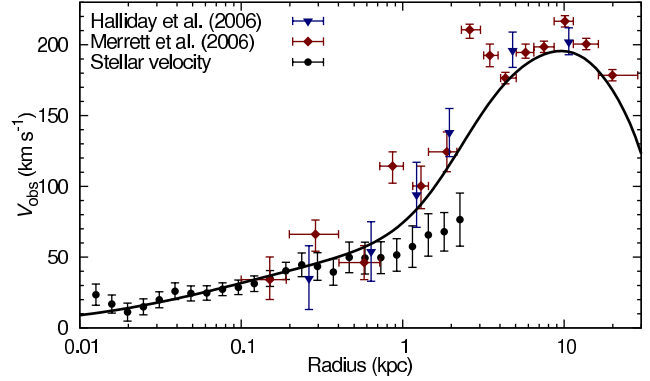


**Figure 7.** PN and stellar velocity along the major axis. The filled triangles and the diamonds are PN rotational velocities, the filled circles are averaged stellar velocities. The solid line is our calculated stellar velocity.

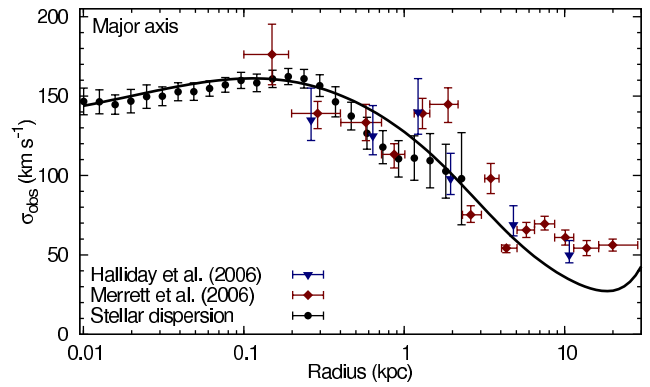


**Figure 8.** Dispersions along the major axis. The filled triangles and the diamonds are PN dispersion observations. The filled circles are averaged stellar dispersions. The solid line is the dispersion from our model.

**Table 2.** Calculated model parameters for stellar components.

Popul.	$L_V$	$a_0$	$q$	$N$	$M/L_V$	$M$	$\beta$
Bulge	1.45	0.64	0.6	4.2	$4.2^{+1.0}_{-1.4}$	3.39	0.25
Disc	2.02	9.3	0.05	0.7	$3.1^{+1.2}_{-0.7}$	5.57	0.98
Halo	0.61	4.0	0.5	2.7	$2.9^{+1.7}_{-0.7}$	1.76	0.4
Dif. halo	0.05	40.0	0.9	2.0	$2.1^{+0.6}_{-0.6}$	0.11	0.3

Masses and luminosities are in units of  $10^{10}M_\odot$  and  $10^{10}L_\odot$  respectively; component radii are in kpc;  $M/L_V$  is expected  $M/L$ -ratio from chemical evolution models and  $M$  is mass used in our dynamical model.

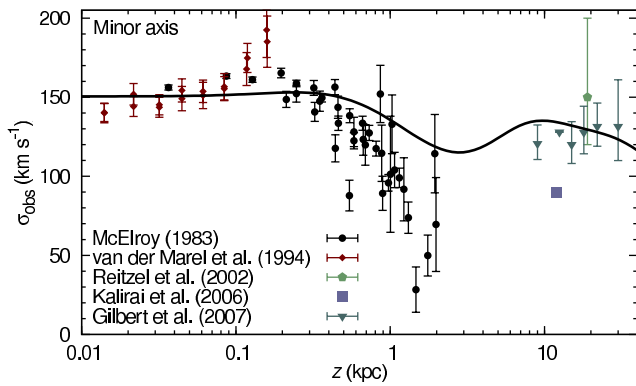


**Figure 9.** Stellar dispersions along the minor axis. The filled circles and the diamonds are stellar dispersions. The pentagon, the square and the triangles are individual RGB stars observations. The solid line is our modelled dispersion.

Stellar rotational velocity is given in Fig. 7. In the inner region ( $R < 0.02$  kpc), the observational velocities are higher than the calculated velocities. M31 has a fast rotating nucleus and the increase of velocities can be explained by using the nucleus. Our model does not include the nucleus and therefore we have a lower velocity profile in this region. The averaged observed stellar rotational velocities in the outer region ( $R > 0.7$  kpc) are smaller than the calculated velocities. We do not have a good explanation for that. However, the observations are very uncertain in this region (see Fig. 4) and some observations are in agreement with our calculated results. We have a satisfactory fit with PN observations. A small disagreement is only in the outer regions, where the calculated velocities are slightly smaller than the observed ones.

Calculated velocity dispersions along the major axis are given in Fig. 8. It is seen that we have a good fit with observations. Only in the outer region ( $R > 5$  kpc, where only PN observations are available) the calculated dispersions are slightly smaller than the observed dispersions. The probable reason for that is that PN observations do not lie exactly along the galactic major axis. The second reason is that the observed dispersions include a component caused by rotation at different positions along the line of sight, which increases the observed dispersions by up to twenty kilometers per second.

Calculated velocity dispersions along the minor axis are presented in Fig. 9. In addition to usual stellar dispersion measurements, we have plotted in Fig. 9 also in-

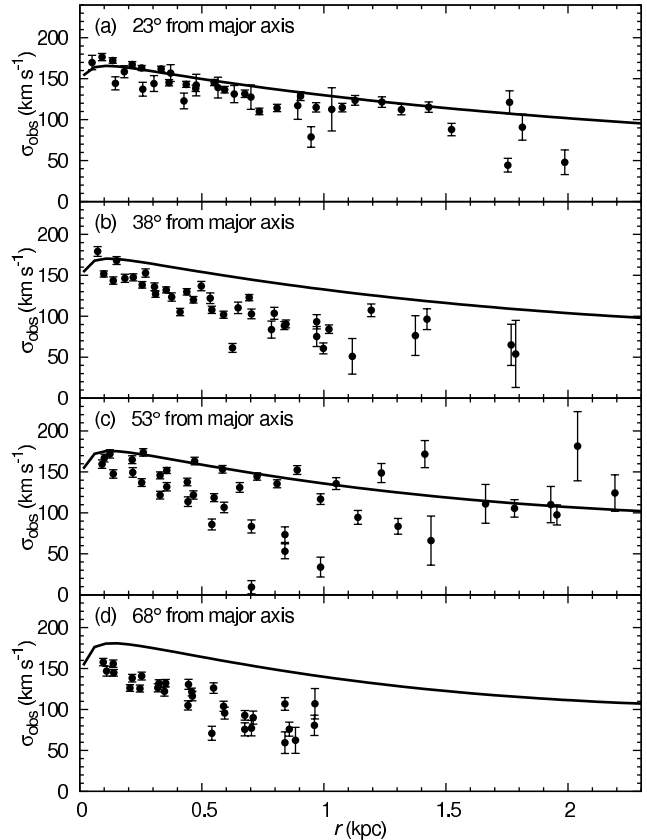


**Figure 10.** Dispersions along slits between the major and the minor axis. The filled circles are dispersions from McElroy (1983). The solid lines are our modelled dispersions. The distance  $r$  is along the slit.

dependent dispersion measurements for RGB stars by Reitzel & Guhathakurta (2002); Kalirai et al. (2006); Gilbert et al. (2007), extending to larger distances  $z$  from the galactic plane. The dispersions calculated from our best-fitting model are in good agreement with observations of RGB stars. In the intermediate regions, the calculated dispersions lie higher than the observed ones. It is possible to have a better fit by using the elliptical DM halo, but still the calculated dispersions are greater than the observed ones.

In Fig. 10 the observed and calculated dispersions along the lines between the major and the minor axis (at  $23^\circ$ ,  $38^\circ$ ,  $53^\circ$  and  $68^\circ$  from major axis) are presented. The observations are with high scatter and they are not symmetric with respect to the galactic centre and are thus uncertain.

## 5 DARK MATTER DISTRIBUTION IN M31

One of the aims of Paper I and the present paper is to derive constraints to the possible DM density distribution and to compare these constraints with several known analytical spherical DM density profiles.

First, we chose for comparison a typical cored density distribution (Burkert 1995)

$$\rho_{\text{Burkert}}(r) = \frac{\rho_0}{\left(1 + \frac{r}{r_c}\right) \left[1 + \left(\frac{r}{r_c}\right)^2\right]}, \quad (29)$$

where  $\rho_0$  is central density and  $r_c$  is characteristic radius.



The cored isothermal density distribution profile is rather similar to the Burkert profile (with the exception of the outer parts) and we left it aside. Next we also used different cuspy density distributions: the Moore profile (Moore et al. 1999)

$$\rho_{\text{Moore}}(r) = \frac{\rho_c}{\left(\frac{r}{r_c}\right)^{1.5} \left[1 + \left(\frac{r}{r_c}\right)^{1.5}\right]}, \quad (30)$$

and the NFW profile (Navarro et al. 1997)

$$\rho_{\text{NFW}}(r) = \frac{\rho_c}{\left(\frac{r}{r_c}\right) \left[1 + \left(\frac{r}{r_c}\right)\right]^2}. \quad (31)$$

In the Moore and NFW profiles,  $\rho_c$  is a density scale parameter.

Later Navarro et al. (2004) have found instead of the NFW profile another density distribution law which fits over a wider distance range. According to Merritt et al. (2006), we refer to this equation as “Einasto’s  $r^{1/n}$  model” (Einasto 1965, 1968, 1969). Following Merritt et al. (2006), we replace the exponent  $\alpha$  in Navarro et al. (2004) equation by  $1/n$

$$\rho_{\text{Einasto}} = \rho_c \exp \left\{ -d_n \left[ \left( \frac{r}{r_c} \right)^{1/n} - 1 \right] \right\}, \quad (32)$$

where  $n$  is in principle a free parameter. According to N-body simulations, we can take  $n = 6.0 \pm 1.1$  (Navarro et al. 2004). The term  $d_n$  is a function of  $n$  in a way that  $\rho_c$  is the density at  $r_c$  defining a volume containing half of the total mass. The value of  $d_n$  can be well approximated by the expression (Merritt et al. 2006)

$$d_n \approx 3n - 1/3 + 0.0079/n. \quad (33)$$

The NFW density profile has extensively been studied and a useful characteristic for this profile is the concentration parameter,  $c_{\text{vir}}$ , defined as the ratio between the virial and inner radii,

$$c_{\text{vir}} \equiv R_{\text{vir}}/r_c. \quad (34)$$

The outer, virial radius  $R_{\text{vir}}$  of a halo of the virial mass  $M_{\text{vir}}$ , is defined as the radius within which the mean density is  $\Delta_{\text{vir}}$  times the critical density of the universe ( $\rho_{\text{crit}} = 3H_0^2/8\pi G$ ):

$$M_{\text{vir}} \equiv \frac{4\pi}{3} \Delta_{\text{vir}} \rho_{\text{crit}} R_{\text{vir}}^3. \quad (35)$$

In the  $\Lambda$ CDM cosmological model, the local value is  $\Delta_{\text{vir}} \approx 337$ .

Using N-body simulations, the correlation between the halo virial mass and the concentration parameter for the  $\Lambda$ CDM model has been found by Bullock et al. (2001); Wechsler et al. (2002). For an Andromeda-sized halo, the concentration parameter is in the range  $10 < c_{\text{vir}} < 20$ . In our model, the concentration parameter is 11.7, which is in accordance with N-body simulations. In principle, in the case of Moore’s law, the concentration index should also be considered. Unfortunately, the dependence of the concentration index of Moore’s law on DM mass is unknown and we cannot take it into account. For the Einasto law, the concentration index in our model is similar to that for NFW law.

Following the scheme presented in Section 3.2, we can estimate the allowed region for the DM density distribution in M 31.

In Fig. 11 the derived DM density distribution as a function of radius is given. To achieve the maximum range in

**Table 3.** Dark matter profiles.

Profile	$\rho_0, \rho_c$ [ $M_\odot \text{pc}^{-3}$ ]	$r_c$ [kpc]	$M_{\text{vir}}$ [ $10^{11} M_\odot$ ]	$R_{\text{vir}}$ [kpc]
Einasto <sup>a</sup>	$1.35 \cdot 10^{-5}$	135.0	7.85	152.7
NFW	$1.74 \cdot 10^{-2}$	12.5	6.93	146.5
Moore	$2.05 \cdot 10^{-3}$	25.0	7.38	149.6
Burkert	$5.72 \cdot 10^{-2}$	6.86	5.16	132.8

<sup>a</sup> Parameter  $n$  has been taken 5.8.

radius, we used three different types of data: stellar observations, PN observations and the gas rotation curve. From kinematical data (Fig. 7 and 8) we see that PN give us the mass distribution in an intermediate range 0.2–20 kpc. Using stellar observations, we can obtain the mass distribution in inner region. In the outer region (up to 35 kpc), we estimate the mass distribution using the gas rotation curve. Using three different types of observations we obtain the DM mass distribution in the range 0.02–35 kpc. The mass distributions derived from PN data have an intersection with stellar and gas data. In interlapping regions all three estimates are in accordance. The error-bars (filled areas) in Figs. 11 and 12 are derived using kinematical observational errors only. The real error-bars are slightly larger, because we must add errors from photometrical observations and intrinsic errors of the model.

Derived in this way density distribution has been fitted with the analytical profiles referred above. Best-fitting profiles are plotted also in Fig. 11 and 12, the corresponding parameters of the profiles are given in Table 3. In addition, virial masses  $M_{\text{vir}}$  and virial radii  $R_{\text{vir}}$  for each profile are given. In our final model (described in the previous section), we have used the Einasto profile.

On the basis of Fig. 11, the inner mass of the DM component was calculated and plotted in Fig. 12 as a function of radius. A number of researchers have used different objects to estimate the total mass inside a given radius or the total mass of M 31. In Table 4 we present some mass estimates at different radii with error-bars. According to Geehan et al. (2006), most reliable estimates are from Evans & Wilkinson (2000), using the PN and the GC data and an estimate by Geehan et al. (2006) on the basis of satellite galaxies. At a distance  $r_{\text{max}} = 125$  kpc three independent mass estimates have been made with the mean value  $7.5 \cdot 10^{11} M_\odot$ . The referred mass estimates in Fig. 12 correspond to dark matter masses: from total masses given in Table 4 the stellar mass was subtracted.

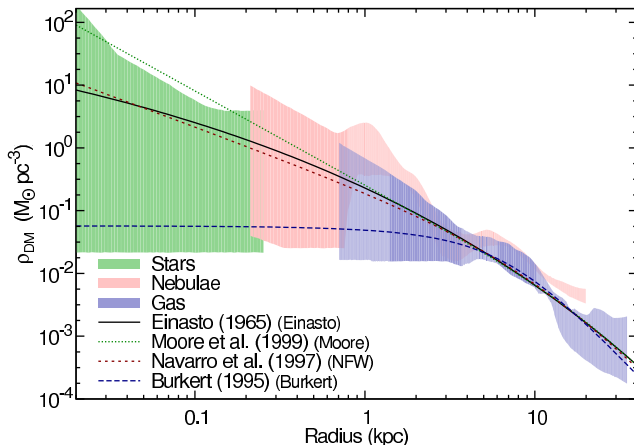
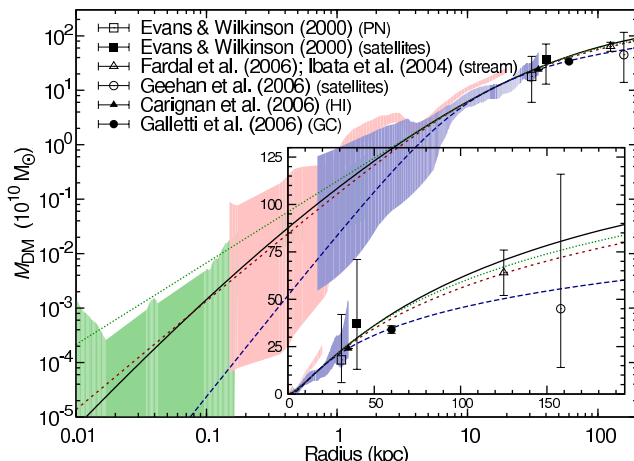
When comparing the derived DM distribution with most common analytical DM density distributions (Figs. 11 and 12), it is seen that within uncertainties nearly all distributions fit with the limits from observations. On the other hand, it is also seen that the Moore profile lies in central regions slightly outside the upper limits of the uncertainties; the Burkert profiles lie rather close to the lower limits of the uncertainties. The Burkert formula predicts also a slightly smaller total and virial mass than the cuspy profiles. It is seen that the NFW and the Einasto density distributions give the best fit.



**Table 4.** Mass estimates for M31 (out to a radius  $r_{\max}$ ).

Reference	$r_{\max}$ [kpc]	Mass [ $10^{10} M_{\odot}$ ]	Objects
Perrett et al. (2002)	27	$41^{+1}_{-1}$	GC
Evans & Wilkinson (2000)*	31	$28^{+24}_{-12}$	PN
Carignan et al. (2006)*	35	34	H I
Evans & Wilkinson (2000)*	40	$47^{+34}_{-23}$	GC
Lee et al. (2008)	55	$55^{+4}_{-3}$	GC
Galletti et al. (2006)*	60	$44^{+2}_{-2}$	GC
Ibata et al. (2004)*	125	$75^{+25}_{-13}$	stream
Chapman et al. (2006)	125	72	RGB stars
Fardal et al. (2006)*	125	$74^{+12}_{-12}$	stream
Geehan et al. (2006)*	158	$55^{+71}_{-31}$	satellites
Evans et al. (2000)	500	$70^{+105}_{-35}$	satellites
Evans & Wilkinson (2000)	total	$123^{+180}_{-60}$	satellites

\* These points are shown in Fig. 12.

**Figure 11.** DM density profile. The filled areas are density profiles derived from stars, PN and gas data. Different lines represent different DM profiles. In our final model we have used the Einasto profile.**Figure 12.** Integrated DM density profile. The filled areas and the lines are the same as in Fig. 11. The points are mass estimates from different authors using different objects.

## 6 DISCUSSION

In Figs. 11 and 12 we tried to estimate all possible uncertainties. The contribution of errors in photometrical surface brightness profiles is small. There is some uncertainty in component subtraction but its influence due to integration along the line-of-sight is relatively small. The most significant uncertainty arises from the stage of using chemical evolution models. First, different colour indices are not in good mutual agreement. Second, chemical evolution models involve several free parameters (initial mass function (IMF), age, star formation duration, contribution of stellar winds etc.). However, it was possible to decrease the influence of all these uncertainties in our final results by using several colour indices ( $U-B$ ), ( $B-V$ ), ( $V-R$ ), ( $R-I$ ) and ( $I-L$ ). In addition, we used independent metallicity measurements allowing us to significantly narrow the possible models. The uncertainties resulting from chemical evolution models were estimated by constructing a large amount of different models with different initial conditions. All this allows us to ascribe errors to the final  $M/L$  and thereafter to the  $M$  values of visible matter for all components (see Table 2).

We derived that within uncertainties nearly all the commonly used analytical DM density profiles fit with limits from observations at nearly all distances. The best-fitting models, however, are the NFW and the Einasto density profiles. Usually in similar studies it is concluded that the NFW profile does not fit with observations.

A common approach in this kind of studies at present is to select galaxies without the bulge component or with a small bulge (see e.g. Simon et al. 2005; Kassin, de Jong & Weiner 2006; Gentile et al. 2004, 2007). The gas rotation curve is corrected for non-circular motions and expansion as well as possible. Colour indices of the disc are derived from surface brightness distributions. Using a colour- $M/L$  relation (usually by Bell & de Jong (2001), updates Bell et al. (2003)) the mass distribution of visible matter is derived. Identifying gas rotation velocities with circular velocities it is possible to calculate the DM density distribution.

To derive the  $M/L$  of visible matter, quite frequently only one or two colour indices are used. This may involve significant uncertainty in the density distribution of visible matter and thereafter in DM.

When modelling S0-Sa-Sbc disc galaxies with a significant bulge component, it is necessary to take into account a detailed luminosity distribution of the bulge and the disc, finite ellipticities of these components, and both the rotation and the dispersion components in stellar kinematics. When ignoring stellar velocity dispersions, the calculated gravitational potential is smaller. Dispersion components in kinematics of a typical spiral galaxy are more dominating in the central parts of the galaxies (see Fig. 13), and thus in the central parts the gravitational potential is underestimated and the resulting DM density profile is flatter near the centre.

Even in a sample of low mass disc, the power-law index in the central regions of galaxies varies highly (Simon et al. 2005). Thus it is worth not to limit DM density studies with bulgeless low surface brightness (LSB) galaxies but to model also galaxies of intermediate and high luminosities and of different morphological types. In LSB and late morphological type galaxies star formation is delayed. This may be

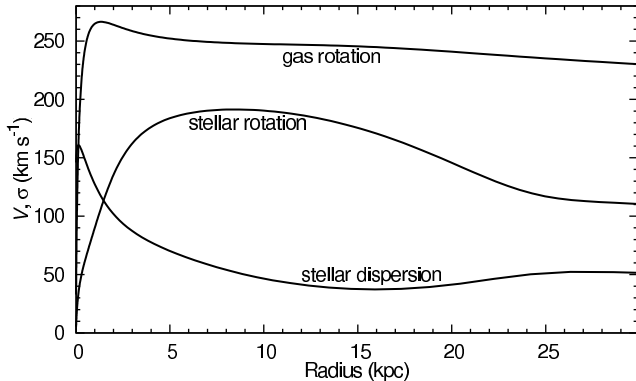


**Figure 13.** Gas rotation, stellar rotation and stellar dispersion components of a typical spiral galaxy as a function of the galactic radius.

caused by insufficiently deep potential well of incompletely formed DM haloes. Thus, it is not surprising that DM density profiles in these galaxies are dominantly not cuspy. In addition, recent study by Pizzella et al. (2008) rises the question about the reliability of the use LSB galaxies as a tracer of mass distribution, in particular in the central regions of LSB galaxies.

Modelled dispersions along the minor axis (Fig. 9) and between the major and the minor axis (Fig. 10) do not have a very good fit with the observed stellar dispersions. Unfortunately, this bulge region has been observed only by (McElroy 1983) and there is a possibility that these observations include some systematic errors that have not been taken into account. On the other hand, our models have several free parameters. In our final model, we use spherical DM density distributions. We have tried elliptical DM profiles and in some aspects the elliptical DM profile gives slightly better results. In our model we have also parameter  $\beta$ , which determines the rotational velocity for stellar components. In our model,  $\beta$  is a constant for each subsystem, but principally  $\beta$  might be a function of  $R$  and  $z$ . As we do not have good quality stellar rotation curves outside the galactic major axis, we do not know how  $\beta$  varies. The last but not least uncertainty in our model is the orientation of the tri-axial velocity ellipsoid. In our model, the velocity ellipsoid is radially elongated and lies under the angles  $\leq 30^\circ$  with respect to the galactic equatorial plane (Tempel & Tenjes 2006). The velocity ellipsoid orientation is quite uncertain and the orientation can affect the modelled dispersions quite significantly. In one of our following papers we analyse this kind of dynamical models in greater detail.

Our derived total mass inside 100 kpc ( $5.6 \cdot 10^{11} M_\odot$  for NFW and  $6.2 \cdot 10^{11} M_\odot$  for the Einasto model) is comparable with mass estimates from Klypin, Zhao & Somerville (2002) ( $8.5 \cdot 10^{11} M_\odot$ ), Geehan et al. (2006) ( $6.0 \cdot 10^{11} M_\odot$ ) and Seigar, Barth & Bullock (2006) ( $6.5 \cdot 10^{11} M_\odot$ ). The ratio of visible matter to total matter (inside 100 kpc) in our model (0.10 for the NFW and 0.092 for the Einasto model) is in good agreement with the results from Klypin et al. (2002) (0.105). On the contrary, the ratios from Geehan et al. (2006) (0.173) and Seigar et al. (2006) (0.152) are somewhat higher than ours: the main difference is that they have almost twice as massive a disc as in our model. Geehan et al. (2006) admit that they have degeneracy between

the disc and dark halo components: reducing the disc mass and increasing the dark halo mass we get better fit with our model. The ratio of the DM mass to the visible mass inside the Holmberg radius ( $\sim 25$  kpc for M31) is 1.75 for the NFW and the Einasto distributions.

The total mass of M31 with the NFW DM distribution is  $1.19 \cdot 10^{12} M_\odot$ , the ratio of the DM mass to the visible mass is 10.0. For the Einasto DM distribution these values are  $1.28 \cdot 10^{12} M_\odot$  and 10.8. Total masses are calculated inside 400 kpc, which is half way from M31 to the Milky Way. The total mass calculated from our model is in good agreement with the total mass calculated by Evans & Wilkinson (2000) on the basis of M31 satellites.

On the basis of the proper motions of the Local Group galaxies IC 10 and M33 and assuming that these galaxies are bound to M31, Brunthaler et al. (2007) calculated a lower limit for the mass of M31 of  $7.5 \cdot 10^{11} M_\odot$ . This mass estimate is in accordance with our mass estimate based on cuspy DM profiles. The cored Burkert profile in our model gives slightly smaller mass than this lower limit.

In central regions the density distribution of the DM can be approximated as  $\rho \sim r^{-\beta}$ . From Fig. 11 we can conclude that  $0 \leq \beta \leq 1.5$ . On the basis of a solution of the Jeans equations Hansen (2004) derived that  $1 \leq \beta \leq 3$ . Resulting common region is rather narrow  $1 \leq \beta \leq 1.5$ .

For local dwarf spheroidal galaxies Gilmore et al. (2007) derived the central characteristic DM density (averaged over a volume of radius 10 pc) within a cusped model  $\sim 60 M_\odot \text{pc}^{-3}$ . For our models, the corresponding values are 33 for the NFW profile and 16 for the Einasto profile. For the cored Burkert profile, this value is  $0.057 M_\odot \text{pc}^{-3}$ . It is interesting to note that the central characteristic density of the DM for cuspy profiles is nearly independent of the galactic mass. This value is close to the upper limit of the central DM density range of nine local galaxies  $(1-4) \cdot 10^{-24} \text{g cm}^{-3} = (0.015-0.059) M_\odot \text{pc}^{-3}$  derived within the cored DM models by Borriello & Salucci (2001). For four galaxies at mean redshifts  $\langle z \rangle \simeq 0.9$ , Tamm & Tenjes (2005) derived the central DM density  $(0.012-0.028) M_\odot \text{pc}^{-3}$ . This lower value at higher redshift may hint to the cosmological evolution of DM densities.

## 7 CONCLUSIONS

In the present paper we have derived the density distribution of DM in a most well-observed nearby disc galaxy, the Andromeda galaxy. In the first part of the study (Paper I), we construct the photometrical model of M31 stellar populations on the basis of surface brightness profiles in  $U$ ,  $B$ ,  $V$ ,  $R$ ,  $I$  and  $L$  colours. The derived photometrical model together with metallicities is used in chemical evolution models to calculate the  $M/L$ -ratios of components. In the second part of the study (the present paper), we construct a consistent mass distribution model of M31. Calculating the rotation velocities and velocity dispersions of visible matter with the help of the dynamical model we found the amount of DM which must be added to reach an agreement with the observed rotation and dispersion data.

We conclude that within uncertainties the Moore, the Burkert, the NFW and the Einasto distributions fit with observational limits at nearly all distances (Fig. 11). How-

ever, it is also seen that in central regions, the Moore and the Burkert profiles lie rather close to the upper and lower limits of uncertainties. The Burkert law does not fit within the lower limit for the mass of M31, set by Brunthaler et al. (2007), either. The NFW and the Einasto density distributions give the best fit.

$\Lambda$ CDM hierarchical clustering theory is in agreement with dark matter density distribution in a well studied disc galaxy M31. Predictions of this theory also agree with observed decrease of disc sizes with redshift (Bouwens & Silk 2002; Ferguson et al. 2004; Tamm & Tenjes 2006).

## ACKNOWLEDGMENTS

The paper has been improved according to the comments of the anonymous referee. We thank Dr. J. Pelt for suggesting the bootstrap method for averaging the observational data. We thank Dr. P. Salucci and Dr. C. Frigerio Martins for pointing out the problem with the NFW concentration parameter. We thank Dr. A.W. Graham for the suggestion to use the Einasto model instead of the Navarro et al. (2004) model. We acknowledge the financial support from the Estonian Science Foundation grants 6106, 7115, 7146 and project SF0060067s08. All figures were made with the GNUPLLOT plotting utility.

## REFERENCES

- Bell E. F., de Jong R. S., 2001, *ApJ*, 550, 212
- Bell E. F., McIntosh D. H., Katz N., Weinberg M. D., 2003, *ApJS*, 149, 289
- Bender R. et al., 2005, *ApJ*, 631, 280
- Binney J., Tremaine S., 1987, *Galactic dynamics*. Princeton Univ. Press, Princeton, NJ
- Blais-Ouellette S., Amram P., Carignan C., 2001, *AJ*, 121, 1952
- Borriello A., Salucci P., 2001, *MNRAS*, 323, 285
- Bouwens R., Silk J., 2002, *ApJ*, 568, 522
- Braun R., 1991, *ApJ*, 372, 54
- Brunthaler A., Reid M. J., Falcke H., Henkel C., Menten K. M., 2007, *A&A*, 462, 101
- Bullock J. S., Kolatt T. S., Sigad Y., Somerville R. S., Kravtsov A. V., Klypin A. A., Primack J. R., Dekel A., 2001, *MNRAS*, 321, 559
- Burkert A., 1995, *ApJ*, 447, L25
- Carignan C., Chemin L., Huchtmeier W. K., Lockman F. J., 2006, *ApJ*, 641, L109
- Chapman S. C., Ibata R., Lewis G. F., Ferguson A. M. N., Irwin M., McConnachie A., Tanvir N., 2006, *ApJ*, 653, 255
- de Blok W. J. G., 2005, *ApJ*, 634, 227
- de Blok W. J. G., Bosma A., 2002, *A&A*, 385, 816
- de Blok W. J. G., McGaugh S. S., Rubin V. C., 2001, *AJ*, 122, 2396
- de Vaucouleurs G., de Vaucouleurs A., Corwin J. H. G., Buta R. J., Paturel G., Fouque P., 1991, *Third Reference Catalogue of Bright Galaxies*. Springer-Verlag Berlin Heidelberg New York
- Einasto J., 1965, *Trudy Inst. Astrofiz. Alma-Ata*, 5, 87
- Einasto J., 1968, *Tartu Astron. Obs. Publ.*, 36, 414
- Einasto J., 1969, *Afz*, 5, 137
- Evans N. W., Wilkinson M. I., 2000, *MNRAS*, 316, 929
- Evans N. W., Wilkinson M. I., Guhathakurta P., Grebel E. K., Vogt S. S., 2000, *ApJ*, 540, L9
- Fardal M. A., Babul A., Geehan J. J., Guhathakurta P., 2006, *MNRAS*, 366, 1012
- Ferguson A. M. N., Irwin M. J., Ibata R. A., Lewis G. F., Tanvir N. R., 2002, *AJ*, 124, 1452
- Ferguson H. C. et al., 2004, *ApJ*, 600, L107
- Galleti S., Federici L., Bellazzini M., Buzzoni A., Fusi Pecci F., 2006, *A&A*, 456, 985
- Geehan J. J., Fardal M. A., Babul A., Guhathakurta P., 2006, *MNRAS*, 366, 996
- Gentile G., Salucci P., Klein U., Granato G. L., 2007, *MNRAS*, 375, 199
- Gentile G., Salucci P., Klein U., Vergani D., Kalberla P., 2004, *MNRAS*, 351, 903
- Gerssen J., Kuijken K., Merrifield M. R., 1995, *MNRAS*, 277, L21
- Gilbert K. M. et al., 2007, *ApJ*, 668, 245
- Gilmore G., Wilkinson M. I., Wyse R. F. G., Kleyna J. T., Koch A., Evans N. W., Grebel E. K., 2007, *ApJ*, 663, 948
- Halliday C. et al., 2006, *MNRAS*, 369, 97
- Hansen S. H., 2004, *MNRAS*, 352, L41
- Ibata R., Chapman S., Ferguson A. M. N., Irwin M., Lewis G., McConnachie A., 2004, *MNRAS*, 351, 117
- Kalirai J. S. et al., 2006, *ApJ*, 648, 389
- Kassin S. A., de Jong R. S., Weiner B. J., 2006, *ApJ*, 643, 804
- Kent S. M., 1989, *PASP*, 101, 489
- Klypin A., Zhao H., Somerville R. S., 2002, *ApJ*, 573, 597
- Kormendy J., 1988, *ApJ*, 325, 128
- Kormendy J., Bender R., 1999, *ApJ*, 522, 772
- Lauer T. R. et al., 1993, *AJ*, 106, 1436
- Lee M. G., Hwang H. S., Kim S. C., Park H. S., Geisler D., Sarajedini A., Harris W. E., 2008, *ApJ*, 674, 886
- McConnachie A. W., Irwin M. J., Ferguson A. M. N., Ibata R. A., Lewis G. F., Tanvir N., 2005, *MNRAS*, 356, 979
- McElroy D. B., 1983, *ApJ*, 270, 485
- Merrett H. R. et al., 2006, *MNRAS*, 369, 120
- Merritt D., Graham A. W., Moore B., Diemand J., Terzić B., 2006, *AJ*, 132, 2685
- Moore B., 1994, *Nature*, 370, 629
- Moore B., Quinn T., Governato F., Stadel J., Lake G., 1999, *MNRAS*, 310, 1147
- Navarro J. F., Frenk C. S., White S. D. M., 1997, *ApJ*, 490, 493
- Navarro J. F. et al., 2004, *MNRAS*, 349, 1039
- Nieten C., Neininger N., Guélin M., Ungerechts H., Lucas R., Berkhuijsen E. M., Beck R., Wielebinski R., 2006, *A&A*, 453, 459
- Peiris H. V., Tremaine S., 2003, *ApJ*, 599, 237
- Perrett K. M., Bridges T. J., Hanes D. A., Irwin M. J., Brodie J. P., Carter D., Huchra J. P., Watson F. G., 2002, *AJ*, 123, 2490
- Pizzella A., Corsini E. M., Sarzi M., Magorrian J., Mendez-Abreu J., Coccato L., Morelli L., Bertola F., 2008, *MNRAS* (accepted), arXiv:0803.2689
- Reitzel D. B., Guhathakurta P., 2002, *AJ*, 124, 234
- Rubin V. C., Ford W. K. Jr., 1970, *ApJ*, 159, 379
- Salow R. M., Statler T. S., 2004, *ApJ*, 611, 245
- Salucci P., Walter F., Borriello A., 2003, *A&A*, 409, 53

- Seigar M. S., Barth A. J., Bullock J. S., 2006, *astro-ph/0612228*
- Simon J. D., Bolatto A. D., Leroy A., Blitz L., Gates E. L., 2005, *ApJ*, 621, 757
- Swaters R. A., Verheijen M. A. W., Bershadsky M. A., Andersen D. R., 2003, *ApJ*, 587, L19
- Tamm A., Tempel E., Tenjes P., 2008, *MNRAS* (submitted), *arXiv:0707.4375* (Paper I)
- Tamm A., Tenjes P., 2005, *A&A*, 433, 31
- Tamm A., Tenjes P., 2006, *A&A*, 449, 67
- Tempel E., Tenjes P., 2006, *MNRAS*, 371, 1269
- Tenjes P., Haud U., Einasto J., 1994, *A&A*, 286, 753
- Unwin S. C., 1983, *MNRAS*, 205, 787
- Valenzuela O., Rhee G., Klypin A., Governato F., Stinson G., Quinn T., Wadsley J., 2007, *ApJ*, 657, 773
- van den Bergh S., 2000, *The Galaxies of the Local Group*. Cambridge University Press, Cambridge
- van der Marel R. P., Rix H. W., Carter D., Franx M., White S. D. M., de Zeeuw T., 1994, *MNRAS*, 268, 521
- Walterbos R. A. M., Kennicutt R. C. Jr., 1987, *A&AS*, 69, 311
- Walterbos R. A. M., Kennicutt R. C. Jr., 1988, *A&A*, 198, 61
- Wechsler R. H., Bullock J. S., Primack J. R., Kravtsov A. V., Dekel A., 2002, *ApJ*, 568, 52
- Weldrake D. T. F., de Blok W. J. G., Walter F., 2003, *MNRAS*, 340, 12
- Zackrisson E., Bergvall N., Marquart T., Östlin G., 2006, *A&A*, 452, 857